Anti-Clockwise Rotation of the Wind Hodograph. Part I: Theoretical Study

M. KUSUDA[1] AND P. ALPERT[2]

Center for Earth and Planetary Physics, Harvard University, Cambridge, MA 02138

(Manuscript received 2 July 1982, in final form 15 October 1982)

ABSTRACT

In a first theoretical study, the reasons for anti-clockwise rotation (clockwise rotation in the Southern Hemisphere) of the wind hodograph in the boundary layer are investigated. As observations of wind hodographs show two different kinds of anti-clockwise rotation (ACR), one frequently observed, which is highly irregular with partly ACR and the other with clear ACR, two methods have been applied. At first a two-dimensional nonlinear model which includes sea-land breezes as well as a mountain reveal partly ACR at the lee of the mountain. By analyzing the different terms in the equation for the wind vector rotation, it is shown that the pressure-gradient term is usually the leading one, and the advection term is very small. But the latter becomes important in cases of ACR. Second, a linear model is solved analytically showing that inclusion of a rotating thermal force in the ACR sense generates clear ACR. It is shown that a critical value for the phase shift between the thermal forces in the horizontal directions exists. At that value, transition to ACR occurs. The critical curves are drawn as function of latitude, friction and relative amplitudes of the thermal forces. Common features of hodographs obtained by observations such as eccentricity, shape, tilt and sense of rotation might be explained in view of the theory.

1. Introduction

An interesting way of presenting wind measurements, as discussed by many investigators, is the hodograph. Some investigators were concerned with changes of wind through the atmosphere, i.e., change of wind with height, as caused by tides, e.g., Wallace and Hartranft (1969). Others studied the hodograph in the boundary layer of the atmosphere or ocean as envisaged through an Ekman layer, e.g., Buajitti and Blackadar (1957) and Endoh and Nitta (1971). The latter hodographs refer to variation of wind with time and our study deals with this kind of hodograph. These latter studies were concerned with a hodograph which is uninfluenced by forcing such as differential heating and topographic features, although Holton (1967) has included the effect of a sloping terrain. In *all* the above studies only clockwise rotation of the hodograph with time was found. A second set of studies discusses the wind hodographs as observed near shores sometimes also influenced by topographic forcing; e.g., Staley (1957, 1958) in northwest Washington; Frizzola and Fisher (1963) in the New York City area; Fosberg and Schroeder (1966) in central California; Weber (1978) in southwestern lower Michigan; Barbato (1978) in Boston; etc. Most of the hodographs (in the Northern Hemisphere) have shown clockwise rotation of wind when observed diurnally at a constant level. But all of those studies mentioned above also show stations with anti-clockwise rotation sometimes quite clear, e.g., the San Francisco Airport as discussed by Fosberg and Schroeder (1966) and shown in Fig. 1. In addition to the observational results, there have been theoretical investigations of land-sea breeze hodographs. Haurwitz (1947) has shown in a highly simplified linear model of the land-sea breezes that the hodographs are ellipses for which rotation is always clockwise. In that work, good agreement was shown with hodograph observations in Boston, although Haurwitz mentioned that anti-clockwise rotation (ACR) is observed as well (Haurwitz, 1947, p. 8). Also, it will be shown later that Defant's (1951) analytical model for the land and sea breezes which includes periodical spatial changes of the horizontal wind predicts only clockwise rotation (CR) in the Northern Hemisphere. Numerical investigation of land and sea breezes in level areas (Neumann and Mahrer, 1971), also show only CR. A numerical calculation by Pielke (1974), which includes more complex forcing such as sea, land and lake breezes in Florida, also generates the ACR (see his Fig. 9 at the northern area of Lake Okeechobee). In addition, Mahrer and Pielke (1977) included land–sea breezes as well as topographic forcing, and obtained a hodograph with partly ACR (see their Fig. 13).

[1] Present affiliation: Oita National Technical College, 870-01, 1666 Oaza-Maki, Oita-City, Japan.

[2] Present affiliation: Cooperative Institute for Mesoscale Meteorological Studies, 815 Jenkins, University of Oklahoma, Norman 73019.

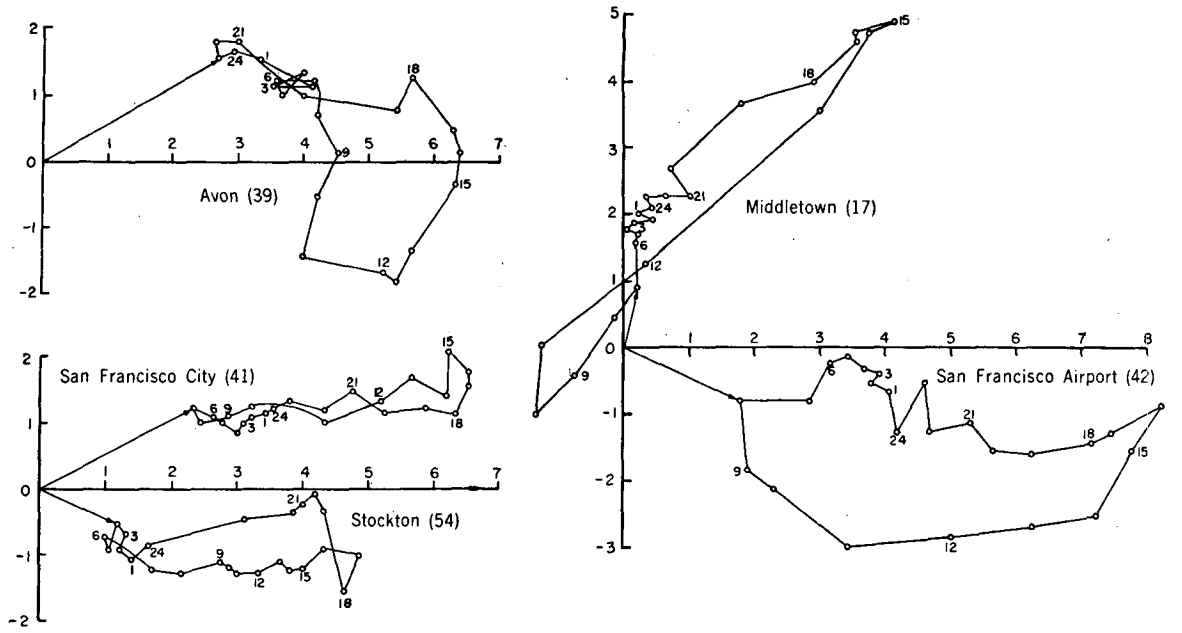

FIG. 1. Hodographs for San Francisco City, San Francisco Airport, Avon, Stockton and Middletown. Units are in m s^{-1}; time is PST. North is at the top of each graph, east is on the right. From Fosberg and Schroeder (1966, Fig. 3). Numbers after name are reference numbers in the original paper.

The direction of rotation is important not only as a purely analytical tool for understanding the boundary layer flow but also may have application to diffusion of pollutants and their possible recirculation as discussed for example by Anthes (1978) and Weber (1978). Thus, the purpose of this paper is to find the required conditions for ACR of the hodograph by a simple analytical model and also by numerical calculations. In the next section, the equation for the rate of wind rotation, following Neumann (1977) and Burk and Staley (1979), and the different terms contributing to rotation rate will be discussed. The numerical approach is adopted in Section 3 in order to estimate the relative importance of these terms when including mountain forcing. Section 4 presents the analytical approach through a simple extension to Haurwitz's theory which does predict ACR under certain conditions. In the last section, the generally observed features of ACR are discussed in view of our results.

2. The equation for the rate of wind rotation

Following Neumann (1977) and the correspondence between Burk and Staley (1979) and Neumann (1979), the equation for the local rate of change of horizontal wind direction may be written as

$$\frac{\partial \alpha}{\partial t} = \frac{1}{V_H^2}\,\mathbf{k}\cdot\left(\mathbf{V}_H \times \frac{\partial \mathbf{V}_H}{\partial t}\right), \tag{1}$$

where α is the angle between the wind vector and the positive direction of x-axis, $\mathbf{V}_H$ is the horizontal wind vector and $\mathbf{k}$ the vertical unit vector. When substituting in the horizontal momentum equation,

$$\frac{\partial \mathbf{V}_H}{\partial t} = -\frac{1}{\rho}\nabla P - f(\mathbf{k}\times\mathbf{V}_H) - \mathbf{V}\cdot\nabla\mathbf{V}_H + \mathbf{F}, \tag{2}$$

where $\mathbf{F}$ represents the frictional force (common notation is used for other terms) then (1) becomes (Lecluyse and Neumann, personal communication, 1980)

$$\frac{\partial \alpha}{\partial t} = -\left(1 - \frac{\mathbf{V}_H\cdot\mathbf{V}_g}{V_H^2}\right)f + \frac{1}{\rho V_H^2}\,\mathbf{k}\cdot(\nabla P_M \times \mathbf{V}_H) + \frac{1}{V_H^2}\,\mathbf{k}\cdot(\mathbf{V}_H\cdot\nabla\mathbf{V}_H \times \mathbf{V}_H) + \frac{1}{V_H^2} \times \mathbf{k}\cdot\left(w\frac{\partial \mathbf{V}_H}{\partial z}\times\mathbf{V}_H\right) - \frac{1}{V_H^2}\,\mathbf{k}\cdot(\mathbf{F}\times\mathbf{V}_H). \tag{3}$$

In this equation the pressure-gradient force has been split into two terms

$$\frac{1}{\rho}\nabla P = \frac{1}{\rho}\nabla P_M - f(\mathbf{k}\times\mathbf{V}_g), \tag{4}$$

where the first term represents the mesoscale pressure gradient and the second the large-scale pressure gradient.

Obviously, the sense of diurnal rotation for the wind hodograph could not be decided through $\partial\alpha/\partial t$, since whenever the origin is not in the hodograph, $\partial\alpha/\partial t$ will change sign as shown in Fig. 2. Accordingly, transformation of coordinates by the average diurnal velocity is necessary unless the origin

is in the ellipse, or when discussing the temporal direction of rotation. Temporal here refers to study of the direction of rotation and the corresponding $\partial\alpha/\partial t$ at a specific time. The rate of rotation in the transformed system is denoted by $\partial\tilde{\alpha}/\partial t$. The direction of diurnal rotation of the hodograph should be decided by $\partial\tilde{\alpha}/\partial t$. Now, referring to Fig. 2, $\partial\tilde{\alpha}/\partial t < 0$ represents diurnal clockwise rotation, while $\partial\tilde{\alpha}/\partial t > 0$ is equivalent to diurnal anti-clockwise rotation. In the following section the relative importance of the different terms on the right-hand side of Eq. (3) will be illustrated through numerical calculation.

3. Influence of mountain forcing on the direction of wind rotation

As shown in many studies on sea–land breezes with two-dimensional (2D) uniformity (i.e., straight coastline and uniform in one horizontal direction), a level region cannot generate ACR. Also, simple 2D sloping terrain leads only to CR as shown by Holton (1967). Including sea–land breezes with a sloping terrain over land again leads to CR in 2D simulations (see, e.g., Asai and Mitsumoto, 1978). In contrast to the aforementioned 2D studies which predict only clear CR, there are many cases of ACR which have been reported for the real atmosphere. A few examples are shown in Fig. 1 in which some hodographs show clear ACR and the others show at least temporary or partly ACR. Therefore, sea–land breezes in conjunction with a mountain near the coast is the case chosen as a "simple" example which may generate ACR ("simple" refers here to the 2D uniformity). We shall illustrate that ACR is indeed possible in this case, and then discuss the relative importance of the terms contributing to the rate of wind rotation from Eq. (3). To start with a simple case, a bell-shaped mountain with 400 m height and a peak at 28 km inland was chosen near the shore.

The model applied for simulating the evolving fields is a two-dimensional σ-system described by Alpert *et al.* (1982). The vertical turbulent transports are calculated through a high-resolution boundary-layer formulation by Blackadar (1978). Turning to the numerical side, a very accurate advection scheme by upstream cubic spline interpolation was adopted as shown, e.g., by Mahrer and Pielke (1978). Explicit horizontal diffusion has been eliminated by the use of a high selective implicit filter proposed by Long *et al.* (1978). For discussion of the advantages of this filter relative to explicit filters see Alpert (1981). Marchuk's (1974) method of splitting was applied in order to permit the use of an efficient implicit method for the vertical diffusion terms. The numerical grid consists of 65 points in the horizontal with a constant spacing of 4 km and 10 levels in the vertical at altitudes of ~10, 20, 40 up to ~2800 m above surface. In the following experiments no large-scale pressure gradient was assumed, and the heating is by prescribing a realistic surface temperature the same as in the study by Alpert *et al.* (1982).

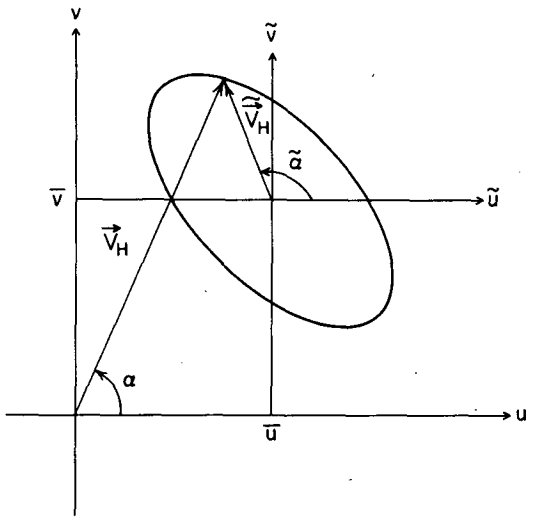

FIG. 2. Transformation of coordinates in defining direction of rotation for the hodograph.

Figs. 3a and 3b show the horizontal wind arrows for 1600 and 0400 (all times LST) the second day of simulation starting at 0800. At 1600, the sea breeze is combined with the mountain wind to generate relatively strong winds uphill, while at the lee side the westerly wind just penetrates and advances toward the weak easterlies. The strong convergence is visualized through the divergence at the upper levels (~1 km). At 0400 katabatic winds downhill are dominant. At the western slope toward the sea, the easterly wind is stronger, relative to the winds at the eastern slope, probably due to the contribution of the land breeze. The general features described so far are very similar to those reported by Mahrer and Pielke (1977).

We now turn to the hodographs—the main concern of this study. Fig. 4 presents the wind vector rotation at the lowest level of the model (~10 m) at the shore. As shown, the integration was performed to the third day and after approximately 9–12 h an effective steady state has been reached.

The rotation of this hodograph shows clear clockwise rotation and that is really not surprising since most researchers pinpoint their numerical hodographs at points near the seashore. In contrast, Fig. 5 illustrates other features of the hodograph; in particular it shows the matrix of 4 × 4 hodographs at four representative points: −36, 0, 16 and 36 km from the seashore and at four different altitude levels. The latter two points are on the two slopes of the mountain, whereas the other points are 36 km offshore and right on the seashore. The hodographs are shown at four model levels (10, 6, 5 and 3), i.e., ~10, 100, 200 and 600 m above the surface. All the hodographs are

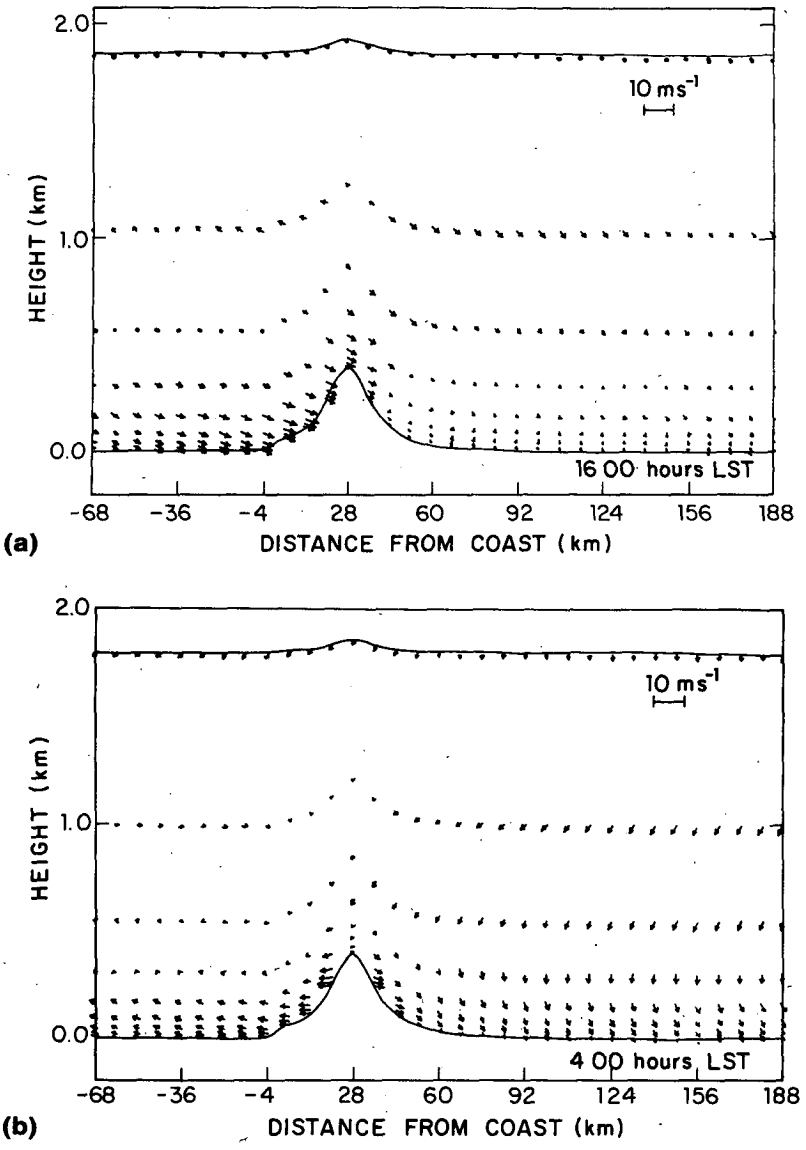

FIG. 3. Horizontal winds over a bell-shaped mountain at (a) 1600 LST, (b) 0400 LST. Arrow bases are fixed at the level which they represent. Direction of arrows to the right represent purely westerly winds, whereas the upward direction indicates southerly winds. The horizontal wind scale is introduced in the upper right corner.

for 25 h, starting at 1000 LST on the second day of simulation. As a general feature, the clear clockwise rotation dominates over the picture. The uncommon hodographs are at the higher level (level 3) and at the point 36 km from the shore. The hodographs at the higher level are not steady enough for careful investigation and this is probably due to reflection from the top boundary. But, at the lee side of the mountain there exists a complex hodograph including partial ACR. This ACR is obtained at the right-hand side of the hodograph corresponding to the hours from afternoon to the following morning. This tendency of the hodograph to have ACR gradually disappears with height, and at level 5 (~200 m) clockwise rotation is obtained. To be sure about this feature of the flow, a second experiment was run with a lower mountain (200 instead of 400 m) with a peak at 48 km from the seashore and the same behavior was obtained. Also, a third experiment with a trapezoidal shape for the mountain gave very similar results. The results from these experiments are thus not shown here. In regard to the common hodographs with clockwise rotation, two known characteristics are observed. First, the smaller hodograph near the ground becomes larger with height and then again diminishes in magnitude up to the level of almost zero wind. This was observed and discussed by Buajitti and Blackadar (1957). A second feature is the higher ec-

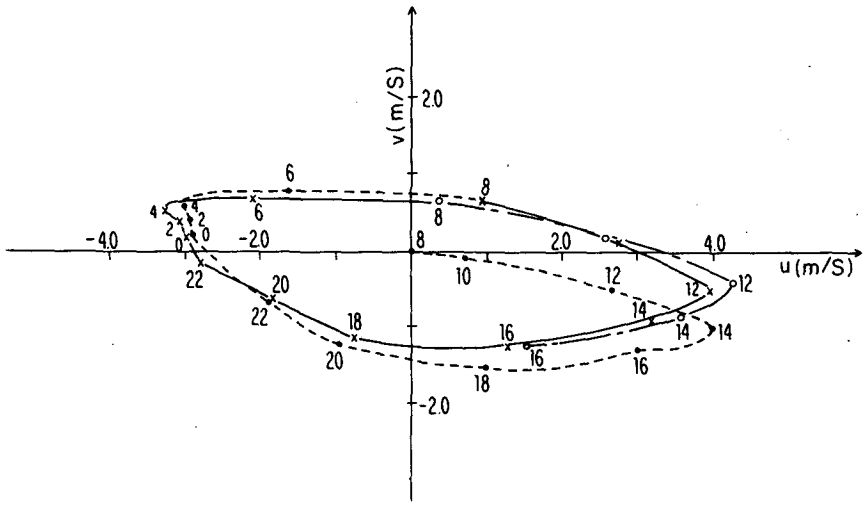

FIG. 4. The hodograph for the first three days of calculations for a point at the shore 10 m above the surface. The numbers near the curve indicate the corresponding hour at LST. First day, dashed line; second day, solid line; third day, dash-dotted line.

centricity of the hodograph ellipse near the shore, relative to that at −36 km offshore. Probably, this is explained by the higher friction near shore and over land as shown by the Haurwitz (1947) theory.

Trying to understand the peculiar hodograph at 36 km inland and the reasons for the tendency toward ACR, the various terms in Eq. (3) have been calculated for 1600. Table 1 summarizes the scaled values for the different terms at the lowest level (~10 m) of the model. Scaling is by Coriolis parameter at

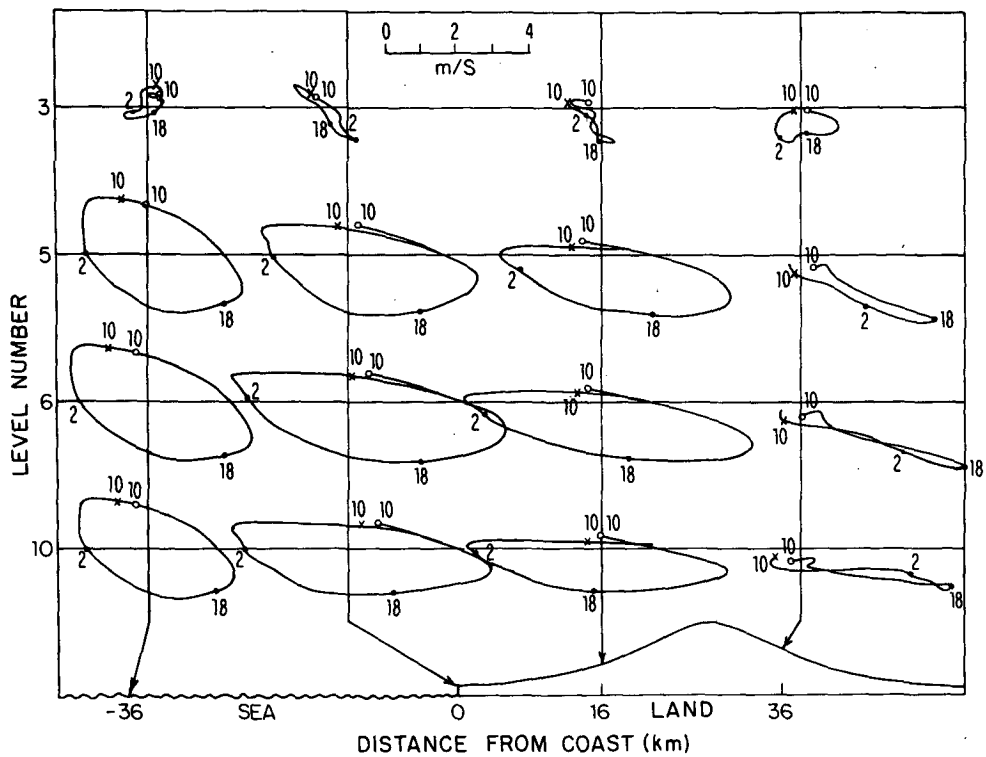

FIG. 5. A matrix of 4 × 4 hodographs from numerical calculation at four representative points: −36, 0, 16 and 36 km from seashore. The surface height is 0, 10, 180 and 250 m, respectively. The four height levels are approximately 10, 100, 200 and 600 m above the surface.

TABLE 1. Values of different terms in Eq. (3) scaled by the Coriolis parameter for four points at the lowest level (for definition of terms, see text).

Distance from the coast (km)	$-f/f$	P/f	AD/f	W/f	FR/f	$\frac{\partial\alpha}{\partial t}/f$
−36	−1	0.65	0.01	0.0	−1.48	−1.82
0	−1	−1.54	0.01	0.0	0.24	−2.29
16	−1	−1.88	−0.0	−0.0	0.19	−2.69
36	−1	4.34	1.52	−0.04	−2.82	2.00

~30°N and the values discussed are

P, the mesoscale pressure-gradient term

$$P = \frac{1}{\rho V_H^2}\,\mathbf{k}\cdot(\nabla P_M \times \mathbf{V}_H);$$

AD, the horizontal advection term

$$AD = \frac{1}{V_H^2}\,\mathbf{k}\cdot(\mathbf{V}_H\cdot\nabla\mathbf{V}_H \times \mathbf{V}_H);$$

W, the vertical advection term

$$W = \frac{1}{V_H^2}\,\mathbf{k}\cdot\left(w\frac{\partial\mathbf{V}_H}{\partial z} \times \mathbf{V}_H\right);$$

FR, the friction term

$$FR = -\frac{1}{V_H^2}\,\mathbf{k}\cdot(\mathbf{F} \times \mathbf{V}_H).$$

The last term FR is due to the vertical eddy stress.

Before discussing the results, two points regarding the calculations are in order. First, since only partial ACR was obtained, it suffices to study the temporal rate of rotation, i.e., $\partial\alpha/\partial t$. Second, no direct calculations of the effect of horizontal smoothing by the implicit filter is possible, and thus it is not shown in the table. However, following some equivalent horizontal diffusion coefficients mentioned by Pielke (1981, p. 268), it was estimated to be less than the frictional term FR for the small filter parameter used.

As immediately observed from Table 1, the most important term is the mesoscale pressure gradient P, and then the frictional term FR, and the Coriolis parameter. Horizontal and vertical advection terms may thus be neglected except for the lee side of the mountain. Turning to the point at the lee side of the mountain, it is clear that the large positive pressure-gradient term P is responsible for the ACR. Burk and Staley (1979) argue that FR is negative when $\partial\alpha/\partial t = 0$. Here it is found that when mesoscale forcing is included, FR might be slightly positive (when the pressure-gradient term P is negative) but in that case, $\partial\alpha/\partial t$ is really not zero (see final column in Table 1). In fact, FR always tends to be in the opposite sign of P, although FR positive values are too small to be capable of changing the sense of rotation to anti-clockwise. The reason for the negligible advection term (AD) was found to be the inter-cancelation of the terms comprising AD, i.e., $v\partial u/\partial x$ and $-u\partial v/\partial x$. This does not happen at the lee side of the mountain (where $\partial v/\partial x$ changes sign), and the larger AD also contributes to the anti-clockwise rotation generated there. The physical reason for that is basically the arrival of the sea breeze to the lee of the mountain. This breeze causes the change from southeasterly mountain wind during noon, to the northwesterly wind associated with the sea breeze.

Table 2 compares the above terms at two points (−36 and +36 km from seashore) and also with a higher level. The values of the different terms are calculated at level 3 (~600 m). The hodographs at 36 km inland change with height from ACR to CR due to a change of sign in P. In addition to the change of sign in P with height, the considerable reduction in FR, as anticipated, is prominent.

In conclusion, the importance of the nonlinear effect to the generation of this kind of weak and temporary ACR has been demonstrated. This became apparent from the relatively large value of the advection term AD, whenever ACR happens to occur. The next section will introduce a different kind of ACR. This will be generated by linear phenomena and appear to be a clear ACR which persists diurnally.

4. A simple analytical example for ACR

In the preceding section it was shown that the horizontal pressure-gradient term makes an important contribution to the rate of rotation (and hence to possible ACR). However, the last section dealt with a very restrictive assumption that there exists uniformity in one horizontal direction. This assumption is quite unrealistic in the atmosphere and, as will be shown later, the inclusion of variations in both directions of the horizontal plane is quite essential for clear ACR. In order to be able to analytically solve the problem when variations in two horizontal directions (x, y) is important, we must assume that one vertical level may represent the changes in the planetary boundary layer (PBL). This is not as restrictive

TABLE 2. As in Table 1, but for two different levels. Levels 10 and 3 correspond to approximately 10 and 600 m above the surface.

Distance from the coast (km)	Level no.	$-f/f$	P/f	AD/f	W/f	FR/f	$\frac{\partial\alpha}{\partial t}/f$
−36	10	−1	0.65	0.01	−0.0	−1.48	−1.82
	3	−1	−1.68	−0.19	−0.37	0.08	−3.16
36	10	−1	4.34	1.52	−0.04	−2.82	2.00
	3	−1	−3.72	0.35	0.0	0.01	−4.35

when strong horizontal forcing dominates the flow. Such an example is found in Haurwitz (1947) for the sea–land breeze circulation. Following Haurwitz we shall also neglect the advection terms in the horizontal momentum equations. Removing the linear advection terms is in fact equivalent to looking for the steady-periodic solution based on the assumption that air parcels have for a long time been subject to the same diurnal pressure gradient. As shown earlier, the contribution to the rate of rotation due to the nonlinear advection terms may usually be neglected. Thus, for the purpose of studying the sense of rotation as influenced by the mesoscale forcing, it does not seem quite so restrictive to neglect all the advection terms in the horizontal momentum equations. This might be true in many cases. But, as shown earlier, sometimes the nonlinear effect is important, for example, at the lee of the mountain. The contribution of the linear advection terms is assumed to be small.

Another important question relates to the severe limitations imposed by linear particle dynamics when applied to atmospheric motions. As indicated by B. Haurwitz (1950), the particle dynamics can only "give a very sketchy indication of the behavior of a fluid since an isolated particle is not restricted by any continuity equation and since its motion does not affect the field of the pressure-gradient force." Also, transient states of the mesoscale circulation are neglected following the treatment by Haurwitz (1947). Nevertheless, it is still possible within our theory to obtain some important conclusions regarding the shape of the hodograph in relation to the diurnal mesoscale forcing.

It should be stressed that in the following derivation, no restriction to the land–sea breeze phenomenon is necessary. In fact, the following theory should be realized as including any possible realistic mesoscale forcing introduced by differential heating such as sea–land and lake–land breezes, mountain–valley winds, differential heating due to different albedo values, etc.

Parameterizing the forces in the horizontal directions by $F_1(t)$ and $F_2(t)$ leads to the following set of horizontal momentum equations in the x and y directions, respectively:

$$\frac{\partial u}{\partial t} - fv + ku = F_x - F_1(t), \tag{5}$$

$$\frac{\partial v}{\partial t} + fu + kv = F_y - F_2(t), \tag{6}$$

where F_x and F_y are the forces due to large-scale pressure gradients. Here k is a constant which expresses the intensity of the frictional force.[3] Following the formula used by Haurwitz for land–sea breeze theory we set

$$F_1(t) = \frac{A}{\pi} + \frac{A}{2}\cos\omega t, \tag{7}$$

$$F_2(t) = \frac{B}{\pi} + \frac{B}{2}\cos(\omega t - \theta), \tag{8}$$

where A and B are forcing amplitudes in the x and y directions, ω is the angular speed of earth's rotation and θ is some phase shift between the two forces. The phase-shift θ is introduced since we are interested in including cases for which the forcing in the x and y directions are not in phase. Such cases are most common in nature whenever two different sources of forcing exist. For example, differential heating due to land–sea effects and to mountainous terrain. As shown later, this phase shift is going to play an important role in ACR. Solution of (5) and (6) leads to u and v terms which consist of constant parts plus oscillating parts with time. What is of concern here is the transformed values $\tilde{u}$ and $\tilde{v}$ (Section 2) which exclude the constant components (see Appendix A):

$$\tilde{u} = \frac{A}{2}\frac{(f^2 - \omega^2 - k^2)\omega \sin\omega t - (f^2 + \omega^2 + k^2)k\cos\omega t}{(f^2 - \omega^2 - k^2)^2 + 4f^2k^2} - \frac{B}{2}2fk\omega \sin(\omega t - \theta) + \frac{(f^2 - \omega^2 + k^2)f\cos(\omega t - \theta)}{(f^2 - \omega^2 - k^2)^2 + 4f^2k^2}, \tag{9}$$

$$\tilde{v} = \frac{A}{2}\frac{2fk\omega \sin\omega t + (f^2 - \omega^2 + k^2)f\cos\omega t}{(f^2 - \omega^2 - k^2)^2 + 4f^2k^2} + \frac{B}{2}\frac{(f^2 - \omega^2 - k^2)\omega \sin(\omega t - \theta) - (f^2 + \omega^2 + k^2)^2 k\cos(\omega t - \theta)}{(f^2 - \omega^2 - k^2)^2 + 4f^2k^2}. \tag{10}$$

The sign of $\partial\tilde{\alpha}/\partial t$ which determines the direction of rotation of wind hodograph is given by

$$\operatorname{sign}\frac{\partial\tilde{\alpha}}{\partial t} = \operatorname{sign}(\sin\theta - C),\ B \neq 0, \tag{11}$$

where

$$C = \frac{A^2 + B^2}{AB}\frac{f\omega}{f^2 + \omega^2 + k^2}. \tag{12}$$

Note that C is always positive for the Northern Hemisphere. This implies that positive $\partial\tilde{\alpha}/\partial t$, which means ACR, is possible only when C becomes less than 1.

[3] Although Burk and Staley (1979) pointed out that the direct contribution to the rotation rate by the Rayleigh friction is zero, it is this form of friction that was chosen from reasons of simplification to the analytical solution.

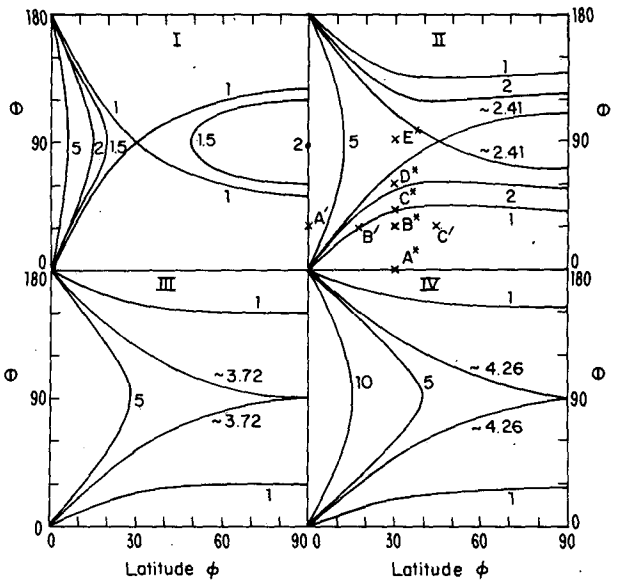

FIG. 6. Curves for critical phase shifts as functions of latitude for different forcing amplitudes: I. $k = 0$, II. $k/\omega = 1$, III. $k/\omega \cong 1.73$, IV. $k/\omega = 2$. The numbers near the curves indicate the relative amplitudes A/B or B/A. Areas closed by curves and vertical axes represent ACR. The points A*–E* and A′–C′ will be referred to later.

If we define this value of C as the sine of a critical phase shift θ_0; i.e., $\sin\theta_0 = C$, the condition for ACR becomes

$$\sin\theta > \sin\theta_0.$$

In our discussion so far, positive C has been assumed, but since in the Southern Hemisphere C is negative, the ACR is favored and the condition for CR is simply $\sin\theta < \sin\theta_0$.

The spatial distribution of clockwise and anticlockwise rotation is shown in Fig. 6. These critical curves as a function of latitude are presented for four cases of friction parameters, $k/\omega = 0$, 1, ~1.7 and 2 (I–IV in Fig. 6, respectively). Regions of ACR are closed by the critical curves and the vertical axes.

For an inviscid model (Case I) the region of ACR is largest at the equator where, in fact, ACR is dominant for all phase shifts. Moving toward 30°N, this region of ACR diminishes gradually although the Coriolis parameter f increases. At 30°N where the Coriolis parameter f becomes equal to ω, a singular point is reached. However, for the viscous solutions (Cases II–IV) the singularity disappears. A common feature for all cases is the strong dependence upon the relative amplitudes of the forcings, i.e., A/B or B/A. When one of these proportions increases, or what is equivalent, one of the forcings reduces, the ACR region diminishes. For example, in the inviscid case when one of the forcings reduces to half of the other (i.e., A/B or B/A equals 2) the poleward region of ACR just disappears. This is shown in Case I by the polar point at the phase shift of 90°.

For Cases I and II, the ACR area increases toward the equator and the pole. But as friction increases, the latitude for which ACR diminishes to zero moves northward and for higher values of friction than $k/\omega \approx 1.729$ (i.e., Case III) the ACR region always diminishes northward as expected with increasing Coriolis parameter. Furthermore, Fig. 6 shows that ACR is favored for the phase shift of 90°. In all cases described, as the phase shift θ moves farther from the $\theta = 90°$ line, there is a tendency toward clockwise rotation. Hence, ACR is favorable when the two forcings become comparable in magnitude or as the phase shift θ between these forcings approaches 90°. To illustrate these features, Figs. 7a and 7b present hodographs for some points referred to in Fig. 6 (Case

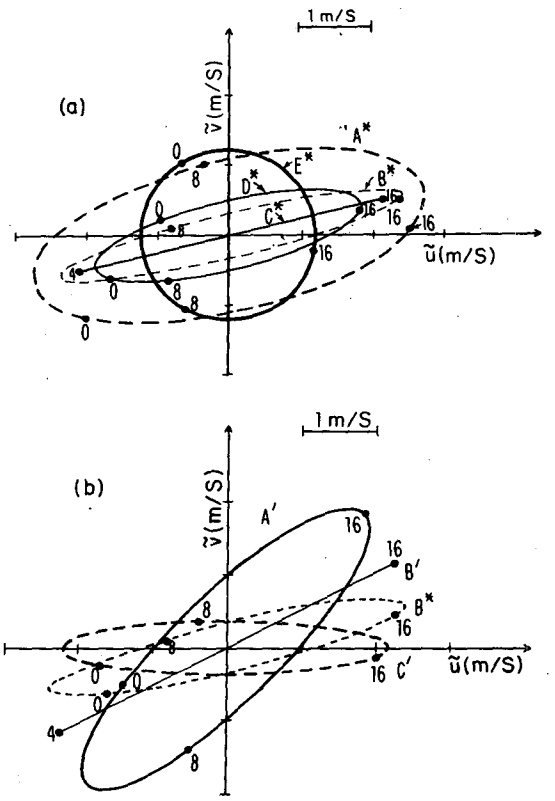

FIG. 7. Some hodographs representing points indicated in Fig. 6, Case II, i.e., $k = \omega$, and for equal forcing amplitudes $A = B = 0.04$ cm s^{-2}. CR is the dashed line, ACR is the solid line. On each hodograph, 3 h are indicated by $t = 0$, 8, 16 h. Time zero corresponds to maximum forcing in the x-direction. (a) For the points A*, B*, C*, D*, E* at latitude 30°N corresponding to phase shifts of $\theta = 0$, 30, ~42, 60 and 90°, respectively. (b) For the points A′, B′, B*, C′ at constant phase shift $\theta = 30°$ corresponding to latitudes of $\phi = 0$, ~18, 30, 45°N, respectively.

II). The value of the friction coefficient for Case II ($k = \omega$) is in agreement with estimations also adopted by Haurwitz (1947) for coastal areas. Thus, we may consider Case II as having a realistic value for friction.

In Fig. 7a, the effect of changing the phase shift on the hodograph's shape is illustrated for a constant latitude of 30°N. As shown for phase shift zero, indicated by the point A*, CR with a large hodograph is predicted. As θ increases, the eccentricity of the ellipse increases up to the point C* just on the critical curve where the ellipse degenerates to a straight line. Further increase in θ brings us to the ACR region and to the point D* with clear ACR. For $\theta = 90°$, the ellipse denoted by E* turns into a circle with ACR. It may be shown that the ACR circle is reached only for A = B and $\theta = 90°$. Also, the tilt of the major axis for the ellipses is constant for the same latitude only for the special case A = B.

As will be discussed later, in nature, the tendency is either toward one dominant forcing, in which case ACR is rare or two comparable forcings with small phase shift between them. Therefore, in the latter case, ACR is difficult to obtain and when it is reached it is usually near the critical curve. In our opinion, this theory suggests the explanation to the high eccentricity found in most of the ACR hodographs reported in the Northern Hemisphere. For that, reference should be made to Fig. 1 and to observations by Staley (1957, his Fig. 3).

The effect of changing the latitude on the hodograph's shape is examined in Fig. 7b for a constant phase shift of 30° and equal forcings A = B. Four hodographs A′, B′, B* and C′ corresponding to latitudes of 0, ~18, 30 and 45°N are depicted. Here again, as in Fig. 7a, points in the ACR region like A′ represent ACR hodographs, whereas B* and C′ outside the ACR region represent CR. Interesting to note is the important influence of latitude in the change of the ellipse's tilt. It should be emphasized that only when the x-forcing *precedes* the y-forcing with the phase shift, i.e., $180° > \theta > 0°$ for our convention, is ACR possible for the Northern Hemisphere. The opposite case when the x-forcing lags cannot lead to ACR. Obviously, this is caused by the earth's rotation as expressed by the Coriolis force.

The domains for ACR and CR over the globe for the full range of phase shifts, i.e., $-180° < \theta < 180°$, is illustrated in Fig. 8. Fig. 8a represents the case where one of the forcings is negligible, corresponding to the Haurwitz (1947) theory. As that forcing becomes larger, areas of ACR and CR appear simultaneously in the northern and southern equatorial region, respectively (Fig. 8b). As the second forcing increases further, more domains of respective rotation appear at the poles (Fig. 8c). However, this stage is missing when friction is relatively high (cf. Fig. 6, Cases III and IV). As both forcings become comparable in magnitude, A = B, contiguous areas from the equator to the pole of ACR and CR are predicted for the Northern and Southern Hemispheres, respectively. These areas, as anticipated, are centered at phase shifts of +90° and −90°, respectively. Thus, in the Northern Hemisphere, ACR is favorable

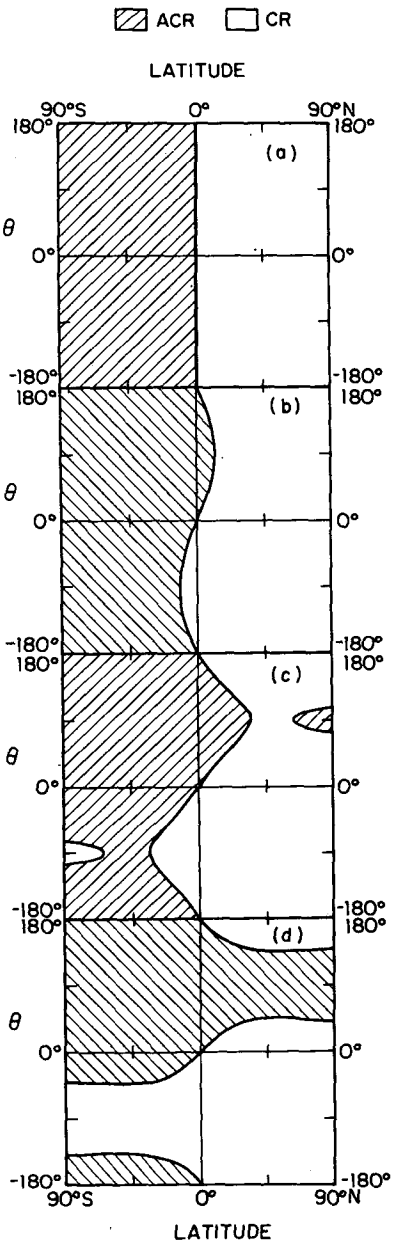

FIG. 8. Representations for domains of ACR and CR over the globe as functions of the phase shift between the forcings for four cases (a)–(d) for which B/A = 0, 0.2, 0.4, 1, respectively. Shaded area represents ACR domain. The friction parameter k is equal to ω.

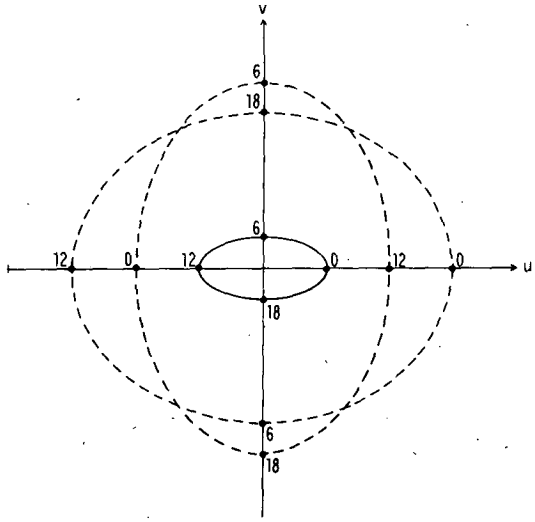

FIG. 9. Schematic illustration of two clockwise rotation wind hodographs (dashed line) and the superposition to an ACR (solid line). The numbers near the curves indicate the corresponding hour in LST.

when the x-forcing precedes the y-forcing with the phase shift; whereas in the Southern Hemisphere, CR is predicted when the x-forcing lags the y-forcing by 90°.

The above condition for ACR may shed light on an empirical rule for ACR in the specific case of mountain–valley circulation. It was observed that orographic left slopes possess ACR, while the opposing right slopes show only CR [see Mass (1982) referring to Hawkes]. (The orographic left slope is on the observer's left as he looks down the valley toward lower elevation.) The interpretation of our conclusion is that the down-valley pressure-gradient force should precede in phase the left-slope mountain force. Of course, when this is the case, the right slope cannot possess ACR. It is interesting to note that we expect this empirical rule to remain valid in the Southern Hemisphere since the condition for CR is turned over. Obviously, our phase shift condition is only a necessary condition and not sufficient; e.g., CR in the Southern Hemisphere is only possible, but not compulsory, on the right slopes there.

An equatorial station like Batavia located at ~6°S will consequently also be influenced by CR as well as ACR domains although only the latter is expected by Haurwitz's theory. That might suggest an explanation of the almost equally observed clockwise and anti-clockwise rotation in Batavia as discussed by Wexler (1946).

The two forcings F_1 and F_2 introduced in this section may be realized as parameterizations for the differential heating near a concave shore which enables two forcings in the x- and y-directions to play a significant role. Alternatively, it may be realized as a case of sea–land breezes associated with lake–land breezes or with mountain–valley winds with comparable forcings.

It should be mentioned that the analytical model for sea–land breezes, as developed by Defant (1951), also predicts only clockwise rotation (see Appendix B) and in light of the foregoing discussion, it is understood. This model as well as those of Haurwitz (1947), Buajitti and Blackadar (1957), and Holton (1967) do not include a second forcing.

5. Discussion and conclusions

In Fig. 1, a few typical ACR hodographs have been shown. One of these hodographs shows clear ACR, the San Francisco Airport; the others show partly ACR. In our study of ACR two different methods have been used. Both lead to two possible reasons for ACR. First, the numerical method for solving the two-dimensional nonlinear set of equations has shown that the nonlinear terms might be partly responsible for ACR at the lee of the mountain.

This kind of ACR is common in the real atmosphere and is usually accompanied by high eccentricity of the hodograph. Such an ACR becomes possible by a delicate balance among the different terms in the equation for the rate of wind rotation. Although the advection term appears to be important for the ACR, the pressure gradient caused by the mesoscale differential heating is in many cases the leading term. Of course, at locations far from appreciable mesoscale forcing, this term becomes less important. It is suggested that the penetration of the sea breeze into the lee region of the mountain is responsible for the ACR during afternoon hours.

A second kind of ACR was introduced in Section 4. This clear ACR, as opposed to the partly ACR mentioned above, was generated by two different forcings in the horizontal plane. It was shown that a phase shift of some critical value between the x- and y-forces is essential for that kind of ACR. This phase shift is a result of the inhomogeneous characteristics of the surface boundary layer. The inhomogeneity is responsible to many of the variations in the thermal forcing involved. The simplest kind of model, widely used, considers the case of a straight coastline, sea or lake, for which maximum forcing occurs around noon. However, when introducing mountainous terrain with different slopes as well as different surface features such as albedo, humidity etc., one usually finds a phase shift between the forcings in one horizontal direction and the other. For example, the temperature difference between two opposing slopes to a valley caused by different angles of solar radiation may reach its maximum in the early morning as shown by Gleeson (1951). Also Staley (1957) in his study of ACR cases in northwest Washington has already anticipated that the shift of the pressure-gradient force to low pressures during the course of the day is the basic reason for ACR. In that

case, Staley assumed that mountain forcing in conjunction with the sea-breeze were responsible to the shift of the pressure-gradient force. In view of this, the reason for the relatively small number of models which predict ACR compared to many observations of ACR, is explained by the lack of consideration to those inhomogeneities which cause the important phase shift.

This critical phase shift value for ACR was found in our study to be a function of friction, latitude and relative amplitudes of the two forces. Also, it was shown that a necessary condition for ACR (CR in the Southern Hemisphere) is the existence of a positive (negative) phase shift θ, $0° < \theta < 180°$ $(-180° < \theta < 0°)$. This condition is equivalent to the requirement that the forcing vector, i.e., $[F_1(t), F_2(t)]$, rotates in the ACR (CR) sense [see Eqs. (7) and (8)]. In other words, if the forcing vector does not rotate, no clear ACR (CR) is possible.

It should be understood that this work does not include the effects on wind rotation due to a variable large-scale pressure gradient and only the possible influence of mesoscale forcing above the sense of wind vector rotation is investigated. As already illustrated by Haurwitz (1947), constant large-scale pressure gradient has no influence above the sense of rotation for linear theory. But, in nonlinear theory, even constant large-scale pressure gradient may affect the sense of rotation temporarily as may easily be shown through Eq. (3) (the third term on the right-hand side).

In Fig. 9 it is clearly shown how two forcings, each of them generating clockwise rotation, may in conjunction cause anti-clockwise rotation. The large ellipses schematically represent the two CR hodographs corresponding to each of the forcings acting alone. They act in conjunction to cause small, but clear anti-clockwise rotation.

Acknowledgments. One of the authors (M.K.) wishes to thank the government of Japan for the support for his stay at Harvard University as a visiting scholar.

This research was supported by the National Science Foundation through Grant ATM 78-23330 and the computing facilities at NCAR.

We wish to express our gratitude to Professor Lindzen for supporting our research at the Center for Earth and Planetary Physics. We wish to thank Professor Neumann and Professor Uryu for their interest and helpful remarks.

APPENDIX A

Derivation of the Formulas (9)–(11)

The set of equations to be solved is

$$\frac{\partial u}{\partial t} - fv + ku = F_x - F_1(t),$$

$$\frac{\partial v}{\partial t} + fu + kv = F_y - F_2(t).$$

Following Haurwitz's derivation, complex notation is introduced. Thus we let

$$\left.\begin{aligned} U &= u + iv \\ F_z &= F_x + iF_y \\ F &= F_1 + iF_2 \end{aligned}\right\}.$$

Then, multiplying the second equation by i and adding it to the first equation yields

$$\frac{dU}{dt} + (k + if)U = F_z - F(t).$$

By integration, the general solution for U is found to be

$$U = \frac{F_z}{k+if} - \frac{1}{\pi}\frac{A+iB}{k+if} - \frac{A}{2}\frac{\omega \sin\omega t + (k+if)\cos\omega t}{\omega^2 + (k+if)^2} - i\frac{B}{2}\frac{\omega \sin(\omega t - \theta) + (k+if)\cos(\omega t - \theta)}{\omega^2 + (k+if)^2} + Ke^{-(k+if)t}.$$

Since the velocity U should vanish if both parts of pressure-gradient force are zero, namely, $F_z = 0$, $A = 0$ and $B = 0$, it follows that $K = 0$.

To obtain the velocity components u and v, the equation for U should be separated to real and imaginary parts leading to

$$u = \frac{kF_x + fF_y}{k^2+f^2} - \frac{1}{\pi}\frac{kA+fB}{k^2+f^2} + \frac{A}{2}\frac{(f^2-\omega^2-k^2)\omega \sin\omega t - (f^2+\omega^2+k^2)k\cos\omega t}{(f^2-\omega^2-k^2)^2 + 4k^2f^2}$$

$$- \frac{B}{2}\frac{2kf\omega \sin(\omega t - \theta) + (f^2-\omega^2+k^2)f\cos(\omega t - \theta)}{(f^2-\omega^2-k^2)^2 + 4k^2f^2},$$

$$v = -\frac{fF_x - kF_y}{k^2+f^2} + \frac{1}{\pi}\frac{fA-kB}{k^2+f^2} + \frac{A}{2}\frac{2kf\omega \sin\omega t + (f^2-\omega^2+k^2)f\cos\omega t}{(f^2-\omega^2-k^2)^2 + 4k^2f^2}$$

$$+ \frac{B}{2}\frac{(f^2-\omega^2-k^2)\omega \sin(\omega t - \theta) - (f^2+\omega^2+k^2)k\cos(\omega t - \theta)}{(f^2-\omega^2-k^2)^2 + 4k^2f^2}.$$

It follows from these expressions for u and v that in the case where $k = 0$ and $f = \omega$, a singular point exists.

Obviously, the sense of clockwise or anti-clockwise hodograph rotation could not be decided by $\partial\alpha/\partial t$, since whenever the origin is not in the hodograph, $\partial\alpha/\partial t$ will change sign (see Fig. 1). Accordingly, we transform coordinates by the average diurnal velocity $\mathbf{V}_H$ and the tilde is chosen for the values in the transformed system:

$$\tilde{u} = u - \frac{kF_x + fF_y}{k^2 + f^2} + \frac{1}{\pi}\frac{kA + fB}{k^2 + f^2},$$

$$\tilde{v} = v + \frac{fF_x - kF_y}{k^2 + f^2} - \frac{1}{\pi}\frac{fA - kB}{k^2 + f^2}.$$

The rotation rate in the transformed system, $\partial\tilde{\alpha}/\partial t$, is given by

$$\frac{\partial\tilde{\alpha}}{\partial t} = \frac{1}{\tilde{u}^2 + \tilde{v}^2}\left(\tilde{u}\frac{\partial\tilde{v}}{\partial t} - \tilde{v}\frac{\partial\tilde{u}}{\partial t}\right),$$

where

$$\tilde{\alpha} = \tan^{-1}\left(\frac{\tilde{v}}{\tilde{u}}\right).$$

After some arrangement, the sign of $\partial\tilde{\alpha}/\partial t$ can be written

$$\operatorname{sign}\left(\frac{\partial\tilde{\alpha}}{\partial t}\right) = \operatorname{sign}[AB(f^2 + \omega^2 + k^2)\sin\theta - (A^2 + B^2)f\omega].$$

APPENDIX B

Rotation Rate in Defants (1951) Theory

The wind components derived by Defant (1951) [see Eq. (19), p. 411] are

$$u = -\frac{r}{(b^2 - a^2)l}M(ae^{az} + be^{-bz})e^{i\omega t}\cos lx,$$

$$v = -\frac{f}{i\omega + k}u.$$

Notation changes for diurnal frequency ω and friction parameter k have been included. Otherwise, notation is according to Defant. In order to get the rotation rate of the wind hodograph, the real parts of the complex solutions u_r and v_r should be picked up:

$$u_r = (m\cos\omega t - n\sin\omega t)\cos lx,$$

$$v_r = \frac{f}{\omega^2 + k^2}[-k(m\cos\omega t - n\sin\omega t) - \omega(m\sin\omega t + n\cos\omega t)]\cos lx,$$

where

$$m + in = -\frac{r}{(b^2 - a^2)l}M(ae^{az} + be^{-bz}).$$

The rotation rate is given as

$$\frac{\partial\alpha}{\partial t} = \frac{1}{u_r^2 + v_r^2}\left(u_r\frac{\partial v_r}{\partial t} - v_r\frac{\partial u_r}{\partial t}\right) = -\frac{\cos^2 lx}{u_r^2 + v_r^2}\frac{f\omega}{\omega^2 + k^2}(m^2 + n^2).$$

In the Northern Hemisphere, the sign of f is positive. Therefore, the sign of $\partial\alpha/\partial t$ is always negative, i.e., only clockwise rotation is predicted by this model independent of height.

REFERENCES

Alpert, P., 1981: Implicit filtering in conjunction with explicit filtering. *J. Comput. Phys.*, **44**, 212–219.

——, A. Cohen, E. Doron and J. Neumann, 1982: A model simulation of the summer circulation from the eastern Mediterranean past Lake Kinneret in the Jordan Valley. *Mon. Wea. Rev.*, **110**, 994–1006.

Anthes, R. A., 1978: The height of the planetary boundary layer and the production of circulation in a sea breeze model. *J. Atmos. Sci.*, **35**, 1231–1239.

Asai, T., and S. Mitsumoto, 1978: Effects of an inclined land surface on the land and sea breeze circulation: A numerical experiment. *J. Meteor. Soc. Japan*, **56**, 559–570.

Barbato, J. P., 1978: Areal parameters of the sea breeze and its vertical structure in the Boston basin. *Bull. Amer. Meteor. Soc.*, **59**, 1420–1431.

Blackadar, A. K., 1978: High resolution models of the planetary boundary layer. *Advances in Environmental and Scientific Engineering*, Vol. 1. Gordon and Breach, 276 pp.

Buajitti, K., and A. K. Blackadar, 1957: Theoretical studies of diurnal wind-structure variations in the planetary boundary layer. *Quart. J. Roy. Meteor. Soc.*, **83**, 486–500.

Burk, S. D., and D. O. Staley, 1979: Comments "On the rotation rate of the direction of the sea and land breezes." *J. Atmos. Sci.*, **36**, 369–371.

Defant, F., 1950: Theorie der Land-und Seewinde. *Arch. Meteor. Geophys. Bioklim.*, **A2**, 404–425.

Endoh, M., and T. Nitta, 1971: A theory of non-stationary oceanic Ekman layer. *J. Meteor. Soc. Japan*, **49**, 261–266.

Fosberg, M. A., and M. J. Schroeder, 1966: Marine air penetration in central California. *J. Appl. Meteor.*, **5**, 573–589.

Fizzola, J. A., and E. L. Fisher, 1963: A series of sea breeze observations in the New York City area. *J. Appl. Meteor.*, **2**, 722–739.

Gleeson, T. A., 1951: On the theory of cross-valley winds arising from differential heating of the slopes. *J. Meteor.*, **8**, 398–405.

Haurwitz, B., 1947: Comments on the sea-breeze circulation. *J. Meteor.*, **4**, 1–8.

——, 1950: Particle dynamics and the sea breeze. *J. Meteor.*, **7**, 164–165.

Holton, J. R., 1967: The diurnal boundary layer wind oscillation above sloping terrain. *Tellus*, **19**, 199–205.

Long, P. E., W. A. Shaffer, J. E. Kemper and F. J. Hicks, 1978: The state of the Techniques Development Laboratory's boundary layer model, 24 May 1977. NOAA Tech. Memo. NWS TDL 66, Silver Spring, MD, 63 pp.

Mahrer, Y., and R. A. Pielke, 1977: The effects of topography on sea and land breezes in a two-dimensional numerical model. *Mon. Wea. Rev.*, **105,** 1151–1162.

——, and ——, 1978: A test of an upstream spline interpolation technique for the advective terms in a numerical mesoscale model. *Mon. Wea. Rev.*, **106,** 818–830.

Marchuk, G. I., 1974: *Numerical Methods in Weather Prediction.* Academic Press, 277 pp.

Mass, C., 1982: The topographically forced diurnal circulation of western Washington State and their influence on precipitation. *Mon. Wea. Rev.*, **110,** 170–183.

Neumann, J., 1977: On the rotation rate of the direction of sea and land breezes. *J. Atmos. Sci.*, **34,** 1913–1917.

——, 1979: Reply. *J. Atmos. Sci.*, **36,** 371.

——, and Y. Mahrer, 1971: A theoretical study of the land and sea breeze circulation. *J. Atmos. Sci.*, **28,** 532–542.

Pielke, R. A., 1974: A three-dimensional numerical model of the sea breezes over south Florida. *Mon. Wea. Rev.*, **102,** 115–139.

——, 1981: Mesoscale numerical modeling. *Advances in Geophysics*, Vol. 23, Academic Press, 185–344.

Staley, D. O., 1957: The low-level sea breeze of northwest Washington. *J. Meteor.*, **14,** 458–470.

——, 1959: Some observations of surface-wind oscillations in a heated basin. *J. Meteor.*, **16,** 364–370.

Wallace, J. M., and F. R. Hartranft, 1969: Diurnal wind variations, surface to 30 kilometers. *Mon. Wea. Rev.*, **97,** 446–455.

Weber, M. R., 1978: Average diurnal wind variation in southwest lower Michigan. *J. Appl. Meteor.*, **17,** 1182–1189.

Wexler, R., 1946: Theory and observations of land and sea breezes. *Bull. Amer. Meteor. Soc.*, **27,** 272–287.